Imaging by parabolic refractive lenses in the hard X-ray range

Bruno Lengeler,[a]* Christian Schroer,[a] Johannes Tümmler,[a] Boris Benner,[a] Matthias Richwin,[a] Anatoly Snigirev,[b] Irina Snigireva[b] and Michael Drakopoulos[b]

[a]*Zweites Physikalisches Institut, RWTH Aachen, D-52056 Aachen, Germany, and* [b]*European Synchrotron Radiation Facility (ESRF), BP 220, F-38043 Grenoble CEDEX, France. E-mail: lengeler@physik.rwth-aachen.de*

The manufacture and properties of compound refractive lenses (CRLs) for hard X-rays with parabolic profile are described. These novel lenses can be used up to ∼60 keV. A typical focal length is 1 m. They have a geometrical aperture of 1 mm and are best adapted to undulator beams at synchrotron radiation sources. The transmission ranges from a few % in aluminium CRLs up to about 30% expected in beryllium CRLs. The gain (ratio of the intensity in the focal spot relative to the intensity behind a pinhole of equal size) is larger than 100 for aluminium and larger than 1000 for beryllium CRLs. Due to their parabolic profile they are free of spherical aberration and are genuine imaging devices. The theory for imaging an X-ray source and an object illuminated by it has been developed, including the effects of attenuation (photoabsorption and Compton scattering) and of the roughness at the lens surface. Excellent agreement between theory and experiment has been found. With aluminium CRLs a lateral resolution in imaging of 0.3 μm has been achieved and a resolution below 0.1 μm can be expected for beryllium CRLs. The main fields of application of the refractive X-ray lenses are (i) microanalysis with a beam in the micrometre range for diffraction, fluorescence, absorption, scattering; (ii) imaging in absorption and phase contrast of opaque objects which cannot tolerate sample preparation; (iii) coherent X-ray scattering.

Keywords: X-ray optics; microanalysis; X-ray imaging; coherent X-ray scattering.

1. Introduction

Microanalysis and imaging with X-rays have developed rapidly over the last few years. They are a major part of the activities at synchrotron radiation sources. Microdiffraction, microfluorescence, microabsorption spectroscopy and X-ray microscopy in absorption and phase contrast have many applications in basic science and technology. While microanalysis requires devices which generate a small focal spot, X-ray microscopy calls for high-quality imaging components. Up to now, curved mirrors (Kirkpatrick & Baez, 1948; Suzuki & Uchida, 1992) and multilayers (Underwood *et al.*, 1986, 1988), single and multiple capillaries (Bilderback *et al.*, 1994; Hoffman *et al.*, 1994) and diffracting lenses (Aristov *et al.*, 1986; Lai *et al.*, 1992; Snigirev, 1995; Snigireva *et al.*, 1998) are the standard means of generating a small focal spot. Some of these devices are suited for imaging (Underwood, 1986; Tarazona *et al.*, 1994; Hartman *et al.*, 1995; Snigirev *et al.*, 1997; Yun *et al.*, 1998). Recently, we have shown that there are means of manufacturing refractive X-ray lenses. Refractive lenses were considered for a long time not to be feasible at all, or at least difficult to fabricate and inferior in quality to Fresnel lenses (Yang, 1993). The first lenses of this type had

cylinder and crossed-cylinder symmetry with a focal length in the metre range and a focal spot size in the micrometre range (Snigirev *et al.*, 1996; Snigirev, Filseth *et al.*, 1998; Elleaume, 1998). A large number of holes, 0.5–1 mm in diameter, are drilled in aluminium or beryllium to form a well aligned row of holes. The material between the holes focuses the beam. Due to the assembly of a large number of individual lenses these refractive X-ray lenses are called compound refractive lenses (CRLs). The concept has also been transferred to the focusing of neutron beams (Eskildsen *et al.*, 1998). However, these lenses show strong spherical aberration and are not well suited for imaging purposes due to imperfections in the lens shaping.

In the meantime, we have considerably improved the concept and the manufacturing of the CRL. The new lenses have a parabolic profile and rotational symmetry around the optical axis. Hence, they focus in two directions and are free of spherical aberration. They are genuine imaging devices, like glass lenses for visible light. They can withstand the full radiation (white beam) of an undulator at third-generation synchrotron radiation sources. The lenses are mechanically robust and easy to align and to operate.

The paper is organized as follows. §2 gives details on the design and on the manufacturing of parabolic CRLs. In §3

Table 1
Typical values of δ and β for beryllium and aluminium as refractive lens material.

Values of X-ray attenuation (photoabsorption and Compton scattering) and of $Z + f'$ from Henke *et al.* (1993).

	Be		Al	
E (keV)	δ (10^{-6})	β (10^{-9})	δ (10^{-6})	β (10^{-9})
8	5.334	2.419	8.579	158.20
10	3.412	1.095	5.468	66.61
15	1.515	0.341	2.414	13.50
20	0.852	0.195	1.355	4.40
30	0.379	0.113	0.601	0.95

we consider the imaging of an undulator source by a CRL. §4 deals with the imaging of an object illuminated by an undulator beam by means of a CRL. A comparison is made between theory and experimental results. Finally, in §5 we give a summary and an outlook on further developments and on applications of the new parabolic CRL.

2. Refractive X-ray lenses

It has been textbook knowledge for many years that there are no refractive lenses for X-rays (Lipson *et al.*, 1998). The lens-maker formula for a convex lens with equal radii of curvature R on both sides reads as

$$1/f = 2(n - 1)/R, \qquad (1)$$

where n is the index of refraction. For visible light in glass, absorption can be neglected and n is ~1.5. In that case a radius of curvature of 10 cm gives a focal length of 10 cm. Hence, many optical designs can be implemented with a single lens. On the other hand the index of refraction n for X-rays in matter reads (James, 1967)

$$n = 1 - \delta - i\beta, \qquad (2)$$

with

$$\delta = (N_A/2\pi)r_0\lambda^2\rho(Z + f')/A, \qquad (3)$$

$$\beta = \lambda\mu/4\pi. \qquad (4)$$

Here, N_A is Avogadro's number, r_0 is the classical electron radius, $\lambda = 2\pi/k_1 = 2\pi c/\omega$ is the photon wavelength, $Z + f'$ is the real part of the atomic scattering factor including the dispersion correction f', A is the atomic mass, μ is the linear coefficient of attenuation and ρ is the density of the lens material. Firstly, the real part of n is smaller than 1. A focusing lens must have a concave form rather than a convex one. Secondly, $1 - \delta$ is very close to 1, δ being of the order of 10^{-6}. Thirdly, although β is a number small compared with 1, X-ray absorption in the lens material is not negligible. This has led to the widespread view that there is no chance of manufacturing refractive X-ray lenses. However, the problems can be overcome by stacking many individual lenses behind one another, by making the radius of curvature small (*e.g.* 0.2 mm) and by choosing a low-Z

lens material (Lengeler *et al.*, 1998; Snigirev, Filseth *et al.*, 1998; Snigirev, Kohn *et al.*, 1998). If, in addition, the profile of the lens is a paraboloid of rotation, spherical aberration can be eliminated (Lengeler *et al.*, 1998, 1999). Under these conditions a focal length of 1 m and a transmission between 1 and 30% can be achieved as shown in this paper. Table 1 shows some typical values of δ and β for materials which are good candidates for refractive X-ray lenses. It turns out that for all energies the β value is much smaller than the δ value.

In Appendix A it is shown that the focal length of a CRL with parabolic profile $s^2 = 2Rw$ (Fig. 1) is

$$f = (R/2N\delta)[1 + O(\delta)], \qquad (5)$$

as measured from the middle of the lens. R is the radius of curvature at the apex of the parabolas, N is the number of individual lenses in the stack. A lens with a thickness $2w_0 + d$ has an aperture $2R_0 = 2(2Rw_0)^{1/2}$ (Fig. 1). For typical values quoted below, in particular for $f \simeq 1$ m, the correction term of order δ in expression (5) is less than 1 mm and will be neglected. Let us consider a typical example. With tabulated f' values (Henke *et al.*, 1993), $\delta = 2.41 \times 10^{-6}$ for aluminium at 15 keV. For a radius of curvature $R = 0.2$ mm we obtain $f = 0.99$ m if $N = 42$. With $2w_0 + d = 1$ mm the lens will have a length of 42 mm,
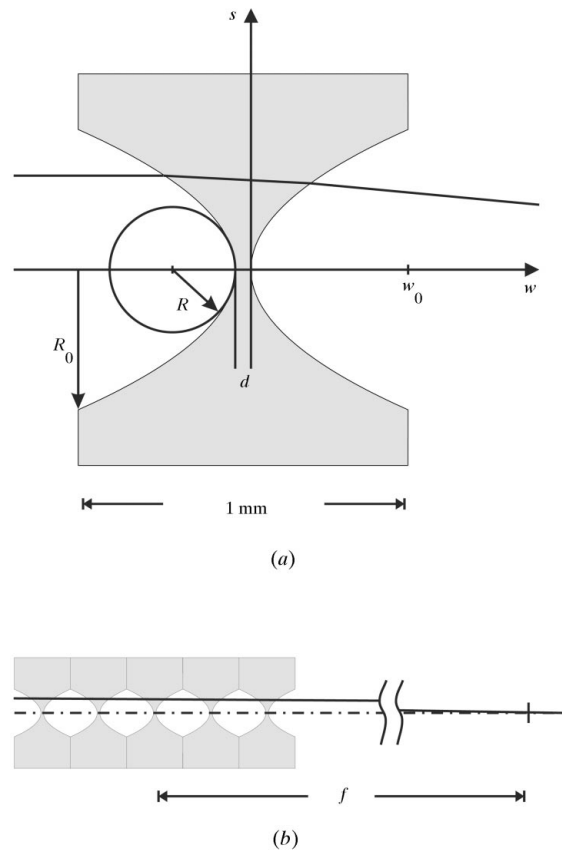

(a)

(b)

Figure 1
Parabolic compound refractive lens (CRL). The individual lenses (*a*) are stacked behind one another to form a CRL (*b*).

which is short compared with the focal length. The lenses described in this paper are made from polycrystalline aluminium by a pressing technique and have been designed and manufactured at the University of Technology in Aachen. The pressing tools consist of two convex paraboloids with rotational symmetry facing each other and guided in a centring ring. The aluminium blank in which the paraboloids are to be pressed from both sides is held and centred by a ring, 12 mm in diameter, that fits tightly into the centring ring. The parabolic lens profile is simultaneously pressed into the aluminium from both sides, in a similar way as metallic money pieces are coined. Modern computer-controlled tooling machines allow the pressing tool to be manufactured with a micrometre precision.

Fig. 2 shows a height profile through one side of a paraboloid as measured by white-beam interferometry. The radius of curvature at the apex of the parabola is $196 \pm 1 \, \mu m$, close to the design parameter $R = 200 \, \mu m$. The surface roughness is about $0.1 \, \mu m$ r.m.s. This will be shown to have a negligible influence on the lens performance. The individual lenses are stacked behind each other by means of two high-precision shafts so that the optical axes are aligned with a precision of $\sim 1 \, \mu m$. An assembled CRL has the size of a matchbox.
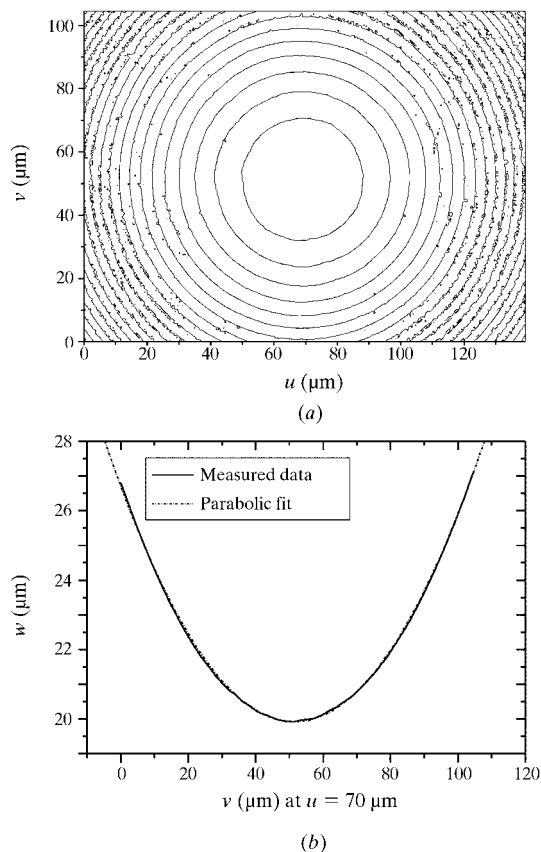
It is very easy to align the lenses in the beam. The lens holder, shown in Fig. 3, has an alignment hole which allows the optical axis at the CRL to be orientated parallel to the synchrotron radiation beam. Once this alignment is performed, the whole lens holder is translated down by 10 mm, so that the beam hits the centre of the lenses. A fine adjustment is performed by means of an Si-PIN diode. The whole alignment takes about 15 min.

In order to test the stability of an aluminium CRL in the white beam of an undulator at the ESRF (50 W) we have measured the temperature as a function of time in the first lens of the stack ($N = 25$) by means of a thermocouple. The CRL was in still air. Fig. 4 shows that the temperature stabilizes below 423 K after 15 min. We conclude that CRLs are able to cope without problems with the heat load from undulators in third-generation synchrotron radiation sources. An additional cooling can easily be applied when the CRLs are intended to be applied in more powerful X-ray beams.

In the following we shall calculate the imaging properties of CRLs, including absorption and surface roughness.
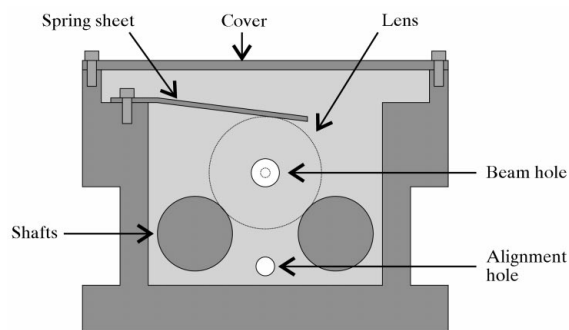

Figure 3
Schematic view of a compound refractive lens.

Figure 2
Height profile of an aluminium lens measured by white-light interferometry; contour plot (*a*) and linear scan through the lens (*b*). The parabolic fit gives $R = 196 \pm 1 \, \mu m$ and a surface roughness of $0.1 \pm 0.1 \, \mu m$ r.m.s.
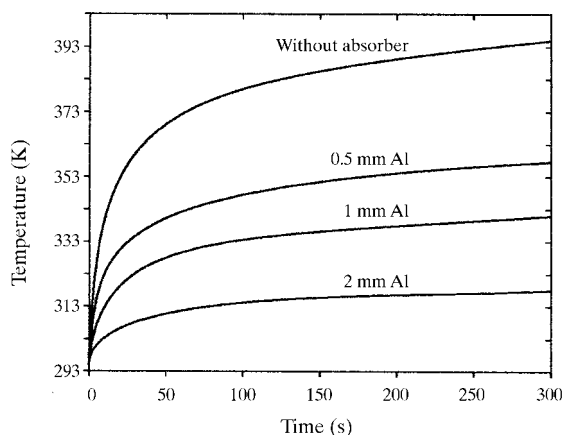

Figure 4
Temperature increase in an aluminium CRL when exposed to the white beam of an ESRF undulator (50 W). Different aluminium absorbers in front of the CRL reduce the power load.

3. Imaging of an undulator source by a CRL

First, we would like to summarize a few properties of undulator sources installed at third-generation storage rings. An undulator source has a finite size described by Gaussians in the vertical and in the horizontal direction,

$$W(x) = (2\pi\sigma_v^2)^{-1/2} \exp(-x^2/2\sigma_v^2), \qquad (6)$$

where σ_v is the r.m.s. width in the vertical direction. There is a similar expression, $W(y)$, for the horizontal direction. At the ESRF a high-β undulator (considered here) has a size $\sigma_v = 14.9\,\mu m$ and $\sigma_h = 297\,\mu m$ which corresponds to a FWHM of $d_v = 35\,\mu m$ in the vertical and $d_h = 700\,\mu m$ in the horizontal. The values quoted here have an uncertainty of at least 10%.

All X-ray sources available at present, including undulators at third-generation synchrotron radiation sources, are chaotic sources because the emission is spontaneous in any mode, rather than stimulated in a well defined fixed mode (Loudon, 1983). An undulator harmonic has a typical bandwidth of 1% at 10 keV. This corresponds to a longitudinal coherence time τ_0 of 4×10^{-17} s. This is the time scale over which the phase of the electric field emitted by one source point undergoes random fluctuations. Even if the beam is monochromated by Bragg reflection to within $\Delta E/E = 10^{-4}$, τ_0 is still only 4×10^{-15} s. This is much shorter than the detector response time of any detector presently available. In other words the intensity measured by any detector is an average over a time much longer than the characteristic time τ_0. The second characteristic feature of the chaotic source is that the phases of the electric field emitted by different source points are uncorrelated. These properties will be used extensively in the following arguments.

Let us consider a CRL with focal length f at a distance L_1 from an undulator. In general the beam passes through a double-crystal monochromator. The monochromatic X-rays should have energy $E = \hbar\omega$ with a bandwidth
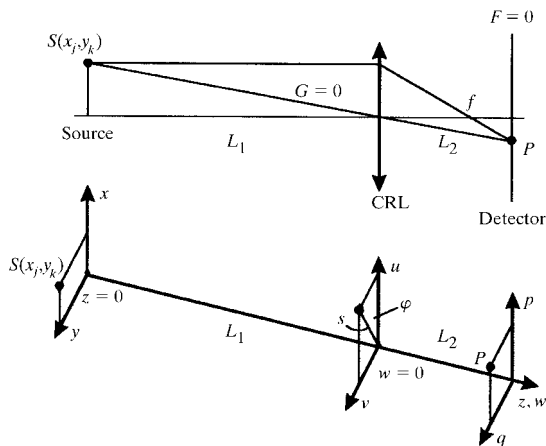
$\Delta\omega = 2\pi\Delta\nu$ much smaller than ω. The X-rays are assumed to be linearly polarized in the horizontal plane. A typical high-β undulator at the ESRF, *e.g.* ID22, has a beam divergence of 25 µrad FWHM. At a distance of 40 m it illuminates homogeneously an object (like a lens) of 1 mm diameter. We ask for the field amplitude $E(t)$ at a given time t at a point P behind the lens (Fig. 5). If we place a detector at P, the number of photons detected during a data-collection time T will be proportional to

$$I = (c/4\pi)\langle|E(t)|^2\rangle = (c/4\pi T) \int_{-T/2}^{T/2} dt\,|E(t)|^2. \qquad (7)$$

The second equality defines the detector average. As mentioned above, the detector collection time is always much longer than the characteristic fluctuation time τ_0 in the phase of the electric field $E(t)$. The field at P is the superposition of the amplitudes emitted by the individual source points and propagating *via* all possible trajectories which pass through the lens. One of these trajectories with an optical path Λ is shown in Fig. 6.

The field amplitudes in the source which contribute to the amplitude at P at time t have to be taken at the retarded time $t - \Lambda/c$. Therefore, each amplitude will contain a factor

$$\exp[-i\omega(t - \Lambda/c)] = \exp(-i\omega t)\exp(ik_1\Lambda), \qquad (8)$$

with $\omega = k_1 c$. Part of the time the photons will propagate in free space (or in air) and part of the time they propagate through the lens material. We denote by t_{12} the amplitude for transmission at an air–lens interface and by t_{21} that at a lens–air interface. So, the amplitude at P at time t for one trajectory is proportional to (Fig. 6)

$$\Phi_{PS} = \exp(-i\omega t)\exp(ik_1\overline{U_iS})(\Phi_L)^N \exp(ik_1\overline{PU_0}). \qquad (9)$$

The amplitude Φ_L for propagation through one lens is given by

$$\Phi_L = \exp\{2ik_1[w_0 + (n-1)w]\}t_{12}t_{21}. \qquad (10)$$

The layer of thickness d (Fig. 1) generates a phase shift which is independent of u, v and is therefore discarded here. However, it is taken into account in the transmission of the lens. In Appendix B it is shown that the transmission amplitude $(t_{12}t_{21})^N$ for N lenses is given by

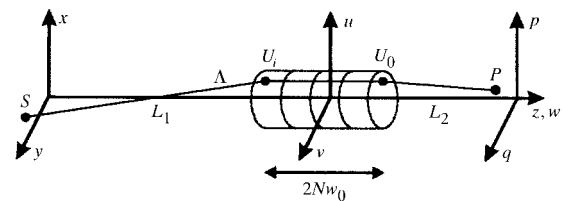$$(t_{12}t_{21})^N = \Delta \exp[-NQ_0^2\sigma^2 s^2/R^2], \qquad (11)$$

Figure 5
Imaging an undulator source S by a CRL (top) and system of coordinates used in the text (bottom).

Figure 6
Trajectory for a photon emitted in S and propagating to P *via* the lens.

$$Q_0 = k_1\delta, \tag{12}$$

$$\Delta = \exp\left[-NQ_0^2\sigma^2\right], \tag{13}$$

where σ is the r.m.s. roughness of a lens surface and Q_0 is the momentum transfer for transmission through an air–lens interface at normal incidence. Since the roughnesses of individual lenses are not correlated, the effective roughness for N lenses with $2N$ surfaces is $(2N)^{1/2}\sigma$. Since refraction is very small and since

$$2R_0, \; 2Nw_0 \ll L_1, \; L_2, \tag{14}$$

we have assumed that the trajectory in the lens is parallel to the optical axis. Hence,

$$\Phi_{PS} = \exp(-i\omega t)\exp\left(ik_1\left\{\left(\overline{U_iS} + \overline{PU_0}\right)\right.\right.$$
$$\left.\left. + 2N[w_0 + (n-1)w]\right\}\right)(t_{12}t_{21})^N. \tag{15}$$

Expansion of $\overline{U_iS}$ to quadratic terms in x_j, y_k, u, v gives

$$\overline{U_iS} = [(u - x_j)^2 + (v - y_k)^2 + (L_1 - Nw_0)^2]^{1/2}$$
$$= L_1 - Nw_0$$
$$+ [(x_j^2 + y_k^2) + (u^2 + v^2) - 2(ux_j + vy_k)]/2L_1. \tag{16}$$

The next term in the expansion of the root gives a contribution to the phase

$$k_1\left[(u - x_j)^2 + (v - y_k)^2\right]^2/\left[8(L_1 - Nw_0)^3\right]. \tag{17}$$

Now, u, v, x_j, y_k are not larger than 500 µm and L_1 is at least 1 m (often 40 m). For 1 Å photons the phase corresponding to expression (17) is smaller than $2\pi \times 10^{-4}$ rad. For this reason higher-order terms in (16) have been neglected. Inserting (17) and the corresponding one for $\overline{PU_0}$ in (15) we obtain

$$\Phi_{PS} = K_j\exp\left[-\alpha s^2 - ik_1Gs\cos(\varphi - \varphi_1)\right], \tag{18}$$

$$K_j = \Delta\exp\left\{-i\omega t + ik_1\left[L_1 + L_2\right.\right.$$
$$\left.\left. + (x_j^2 + y_k^2)/2L_1 + (p^2 + q^2)/2L_2\right]\right\}, \tag{19}$$

with

$$2\alpha R^2 = \mu NR + 2NQ_0^2\sigma^2 - ik_1FR^2 \equiv a - ibF, \tag{20}$$

$$a = \mu NR + 2NQ_0^2\sigma^2, \qquad b = k_1R^2,$$

$$u = s\cos\varphi, \qquad v = s\sin\varphi, \tag{21}$$

$$x_j/L_1 + p/L_2 = G\cos\varphi_1, \qquad y_k/L_1 + q/L_2 = G\sin\varphi_1, \tag{22}$$

$$F = 1/L_1 + 1/L_2 - 1/f, \tag{23}$$

$$G^2 = (x_j/L_1 + p/L_2)^2 + (y_k/L_1 + q/L_2)^2. \tag{24}$$

Summing over all trajectories through the lens results in an integral over φ from 0 to 2π and over s from 0 to R_0, giving

$$\Phi_{PS} = K_j\Gamma, \tag{25}$$

$$\Gamma = \int_0^{R_0} ds\, 2\pi s\exp(-\alpha s^2)J_0(k_1Gs). \tag{26}$$

Before solving the integral we will consider a few interesting special cases.

3.1. Case 1: large transparent CRL

If absorption and roughness are zero ($\mu = 0$ and $\sigma = 0$), the integral equation (26) reads

$$\Gamma = 2\pi\int_0^{R_0} ds\, s\exp(ik_1Fs^2/2)J_0(k_1Gs), \tag{27}$$

and can be solved by the method of stationary phase (Jackson, 1975). The stationary points of the phase are at $s = 0$ and $F = 0$. The point $s = 0$ does not contribute to the integral because $sJ_0(k_1Gs) = 0$. Therefore $F = 0$ is the relevant solution. In other words we expect everywhere destructive interference, except for $F = 0$,

$$\Gamma = 2\pi\int_0^{R_0} ds\, sJ_0(k_1Gs) = 2\pi R_0J_1(k_1GR_0). \tag{28}$$

The Bessel function J_1 of order 1 fluctuates strongly if R_0 is large. When averaged over a finite detector size the amplitude vanishes, unless $G = 0$, in which case $\Gamma = \pi R_0^2$. We conclude that if R_0 is large, if absorption and roughness are zero, we expect a *point to point* imaging by the lens, given by the intersection of the plane $F = 0$ at a distance L_2 equal to

$$L_{20} = fL_1/(L_1 - f), \tag{29}$$

and the ray $G = 0$, *i.e.*

$$x_j/L_1 + p/L_2 = 0, \qquad y_k/L_1 + q/L_2 = 0. \tag{30}$$

This is a result well known from optics textbooks.

3.2. Case 2: very small aperture $2R_0$ (pinhole)

When R_0 is very small, the effect of absorption and roughness is negligible and the phase factor in (26) can be expanded to terms linear in s^2 giving

$$\Gamma = 2\pi\int_0^{R_0} ds\, s(1 + ik_1Fs^2/2)J_0(k_1Gs). \tag{31}$$

The oscillating Bessel function in combination with a finite detector size makes the integral vanish, unless $G = 0$. In other words a pinhole generates intensity everywhere on the ray $G = 0$ (point-to-line imaging), resulting in a very large depth of field. The expansion of the phase factor is justified if R_0 is much smaller than the radius of the first Fresnel zone. The same point-to-line imaging is produced if the absorption in the lens is so large that the effective aperture becomes small. We will now show that real CRLs have a behaviour between the two extreme cases of point-to-point and point-to-line imaging. It turns out that a large depth of field is a characteristic feature of refractive X-ray lenses. We have found no way to solve equation (26) analytically. However, for most practical cases, R_0 is chosen so large that

$$a_p \equiv aR_0^2/2R^2 \gg 1. \tag{32}$$

Then, the upper limit of the integral can be replaced by infinity and the integral can be solved analytically (Abramowitz & Stegun, 1972),

$$\Phi_{PS} = K_j(2\pi/2\alpha) \exp(-k_1^2 G^2/4\alpha). \tag{33}$$

This is (apart from an irrelevant proportionality constant) the field amplitude in P at time t generated by a monochromatic point source in (x_j, y_k) and transmitted through all possible trajectories through the CRL.

We now have to consider the effect of the finite bandwidth of the quasi-monochromatic light. According to expression (8), the field amplitude in P at time t is now proportional to

$$\int d\omega\, g(\omega) \exp[-i\omega(t - \Lambda/c)], \tag{34}$$

where $g(\omega)$ is the frequency distribution of width $\Delta\omega$ for the quasi-monochromatic light. The intensity I measured by a detector at P [see equation (7)] is proportional to

$$\langle|H|^2\rangle \equiv \int d\omega\, d\omega' \Big\{ g(\omega)g^*(\omega') \exp[i(\omega - \omega')\Lambda/c]$$
$$\times (1/T) \int_{-T/2}^{T/2} dt \exp[-i(\omega - \omega')t] \Big\}. \tag{35}$$

The complex conjugate of a quantity is marked by an asterix. As mentioned above, even for a beam monochromated to within $\Delta E/E = 10^{-4}$ the characteristic fluctuation time τ_0 is 4×10^{-15} s, which is much shorter than the fastest detector response. So, the phase $(\omega - \omega')T$ is approximately $2\pi T/\tau_0$ which is much larger than 1 and the time integral in equation (35) can be replaced by $2\pi\delta(\omega - \omega')$, giving

$$\langle|H|^2\rangle = (2\pi/T) \int d\omega |g(\omega)|^2 |\Phi_{PS}|^2. \tag{36}$$

In other words, when the detector collection time is much longer than the characteristic fluctuation time τ_0 then it is the intensities (and not amplitudes) for different frequencies which have to be added. Therefore, for the time being, we consider a monochromatic field $E(t)$ and include the effect of the finite frequency bandwidth later, if needed.

Finally, we have to include the effect of the extended chaotic source with the dimensions quoted in equation (6). This feature is taken into account by including in equation (33) a phase factor $\exp[i\Psi_v(x_j t) + i\Psi_h(y_k t)]$ and summing over the different emitters (j, k) in the source. The phases $\Psi_v(x_j t)$ and $\Psi_h(y_k t)$ fluctuate statistically from source point to source point since the individual emitters in a chaotic source are independent of each other. The field amplitude at the observation point P at time t reads

$$\Phi_P(p, q) = (2\pi/2\alpha) \exp(-i\omega t)\Delta \exp[ik_1(L_1 + L_2)]$$
$$\times \exp[ik_1(p^2 + q^2)/2L_2]\Gamma_v\Gamma_h, \tag{37}$$

$$\Gamma_v = \sum_j \exp(ik_1 x_j^2/2L_1) \exp[i\Psi_v(x_j t)]$$
$$\times \exp\Big[\big(-k_1^2\alpha^*/4|\alpha|^2\big)\big(x_j/L_1 + p/L_2\big)^2 \Big], \tag{38}$$

and similarly for Γ_h. The intensity measured by the detector is again proportional to the modulus squared of Γ_v and Γ_h, averaged over the detector collection time T,

$$\langle|\Gamma_v|^2\rangle = \sum_{jj'} h(x_j)h^*(x_{j'})$$
$$\times \langle\exp\{i[\Psi_v(x_j t) - \Psi_v(x_{j'} t)]\}\rangle, \tag{39}$$

where $h(x_j)$ denotes the remaining factors in the integrand of (38). For a given pair j, j' of emitter coordinates the phase difference in the exponent of (39) fluctuates within the range $0-2\pi$ in the time scale τ_0. If the detector collection time T is much longer than τ_0 the contribution averages to zero, unless $j = j'$,

$$\langle\exp\{i[\Psi_v(x_j t) - \Psi_v(x_{j'} t)]\}\rangle = \delta_{jj'}. \tag{40}$$

In other words, for a chaotic X-ray source, and for $T \gg \tau_0$, the contribution of the individual source points have to be added incoherently,

$$\langle|\Gamma_v|^2\rangle = \sum_j \exp\Big\{[-k_1^2\Re(\alpha)/2|\alpha|^2](x_j/L_1 + p/L_2)^2\Big\}$$
$$= \int dx\, W(x) \exp\Big\{[-k_1^2\Re(\alpha)/2|\alpha|^2]$$
$$\times (x_j/L_1 + p/L_2)^2\Big\}. \tag{41}$$

In the last line we have replaced the sum over the individual emitters by an integral with the Gaussian distribution $W(x)$ given by equation (6). The integral can be solved analytically. Including the similar contribution for $\langle|\Gamma_h|^2\rangle$ we obtain for the intensity at P,

$$I(p, q) \equiv \langle|\Phi_P|^2\rangle$$
$$= \pi^2\Delta^2/[(aa_v + b^2F^2)(aa_h + b^2F^2)]^{1/2}$$
$$\times \exp\Big\{(-ak_1^2 R^2/L_2^2)[p^2/(aa_v + b^2F^2)$$
$$+ q^2/(aa_h + b^2F^2)]\Big\}, \tag{42}$$

$$a_v = a + 2k_1^2 R^2\sigma_v^2/L_1^2, \qquad a_h = a + 2k_1^2 R^2\sigma_h^2/L_1^2. \tag{43}$$

A word should be said about the loss of observability of interference for the field amplitudes emitted by different source points in a chaotic source. It is not exclusively a property of the source, but also a consequence of the slow speed of the detectors (presently) available and of the long detector collection time chosen (long compared with τ_0). In a similar way it was the finite detector spatial resolution which was responsible for the non-observability of intensity outside the ray $G = 0$ in (28) and (31).

Equation (42) is the central expression for the imaging of an undulator source by a CRL. We will now discuss the intensity distribution at the point P with coordinates (p, q, L_2).

3.2.1. *Intensity in the focal plane F = 0.* The focal plane $F = 0$ ($1/L_1 + 1/L_{20} = 1/f$) is at a distance $L_{20} = L_1 f/(L_1 - f)$ from the middle of the lens. In this plane the intensity is distributed according to a Gaussian with width (FWHM)

$$B_v = 2.355 \, L_{20}(\sigma_v^2/L_1^2 + a/2k_1^2 R^2)^{1/2}, \qquad (44)$$

and a similar expression B_h for the horizontal, with σ_v being replaced by σ_h. There are two contributions to B_v. The first one is due to the demagnification of the source according to geometrical optics and is given by (44) for $a = 0$ (*i.e.* for $\mu = 0$ and $\sigma = 0$). It has the value $2.355 \, \sigma_v L_{20}/L_1$. The other term including a [equation (20)] describes the influence of diffraction by the effective aperture of the lens.

3.2.2. *Effective lens aperture D_{eff} and influence of lens surface roughness.* The effective lens aperture can be deduced from the integral equation (26). For $F = 0$ and $G = 0$, the integral has the meaning of an effective lens area. When μ and σ are zero ($a = 0$) the integral has the value πR_0^2. With non-vanishing values of μ and σ the integral is equal to

$$(\pi/4)D_{eff}^2 = \pi R_0^2[1 - \exp(-a_p)]/a_p, \qquad (45)$$

giving, for the effective aperture D_{eff},

$$D_{eff} = 2R_0\{[1 - \exp(-a_p)]/a_p\}^{1/2}, \qquad (46)$$

$$a_p = aR_0^2/2R^2. \qquad (47)$$

For visible light and glass lenses in which absorption and roughness are negligible ($a_p = 0$), the effective aperture D_{eff} is identical to the geometric aperture $2R_0$. Not so for refractive X-ray lenses: here attenuation of the X-rays in the lens material is the limiting factor for the effective aperture. Another comment is appropriate about the influence of roughness on the performance of X-ray mirrors as opposed to X-ray lenses. Roughness reduces the reflectivity and the transmission according to an exponential factor $\exp(-2Q^2\sigma^2)$. For a mirror, the momentum transfer Q is $2k_1\theta$ with a typical value of $0.1°$ for the angle of reflection θ. For $\lambda = 1$ Å, $Q = 2.2 \times 10^{-2}$ Å^{-1}. For an aluminium CRL at 12.4 keV with $\delta = 3.54 \times 10^{-6}$, $f = 1$ m, $N = 28$, the momentum transfer is $(2N)^{1/2}k_1\delta = 1.7 \times 10^{-4}$ Å^{-1}. The low value of Q_0 for a CRL allows for much larger values of σ. If a mirror for hard X-rays needs a surface finish of 1 nm r.m.s., a CRL needs a finish of 1 µm. This is a dramatic difference which simplifies drastically the requirements for manufacturing refractive X-ray lenses.

3.2.3. *Transmission and gain of a CRL.* The transmission of a CRL with N individual lenses and a thickness d between the apices of the parabolas (Fig. 1) is

$$T_p = \exp(-\mu Nd)(1/R_0^2)\int\limits_0^{R_0} ds \, 2s \exp(-as^2/R^2)$$

$$= \exp(-\mu Nd)(1/2a_p)[1 - \exp(-2a_p)]. \qquad (48)$$

For good quality lenses the influence of surface roughness is a minor contribution to a (see below). Then a_p can be expressed in terms of the mass absorption coefficient μ/ρ and of the focal length f as

$$2a_p = (\mu/\rho)(\pi R_0^2/f)\{A/[N_a r_0 \lambda^2(Z + f')]\}. \qquad (49)$$

For a given focal length f and a given photon wavelength λ the transmission of the lens increases with decreasing mass absorption coefficient, *i.e.* low-Z elements as lens material, like Li, Be, B, C and even Al are favourable. In Fig. 7 are shown the mass absorption coefficients of these elements and of Ni. The values μ/ρ first drop with photon energy, as E^{-n} with n close to 3. However, at ~ 0.2 cm^2 g^{-1} the strong decrease merges into a much slower decrease when Compton scattering exceeds photoabsorption. Compton-scattered photons do not contribute to the image formation. Those which are scattered under a large angle are ultimately destroyed by absorption whereas those which are scattered in the forward direction will contribute to a blur of the focal spot. It turns out that Compton scattering ultimately limits the transmission and the resolution of a CRL. The gain of a CRL is defined as the ratio of the intensity in the focal spot and the intensity behind a pinhole of size equal to the spot of the lens. It is (Lengeler *et al.*, 1998)

$$g_p = T_p(4R_0^2/B_v B_h), \qquad (50)$$

where B_v and B_h are the FWHM size of the focal spot in the vertical and horizontal directions.

3.2.4. *Comparison with experimental data.* We have imaged the ID22 source at ESRF with an aluminium CRL and 15 keV (0.83 Å) photons. The lens parameters are $N = 33$, $R = 200$ µm, $2R_0 = 0.87$ mm, $\sigma = 0.1 \pm 0.1$ µm, $\delta = 2.41 \times 10^{-6}$, $\mu = 20.52$ cm^{-1}, $L_1 = 63.00 \pm 0.05$ m. The values for R and $2R_0$ are the same throughout the whole article. For this set of parameters, $\mu NR + 2Nk_1^2\sigma^2\delta^2 = a = 13.54 \pm 0.47 + 0.02 \pm 0.03 = 13.58 \pm 0.50$, $a_p = 32.12 \pm 5.74$, $f = 1.26 \pm 0.04$ m, $L_{20} = 1.29 \pm 0.04$ m, $D_{eff} = 154 \pm 10$ µm. It is obvious that the roughness of 0.1 µm in the lens surface gives a minor contribution to a_p and hence to the effective
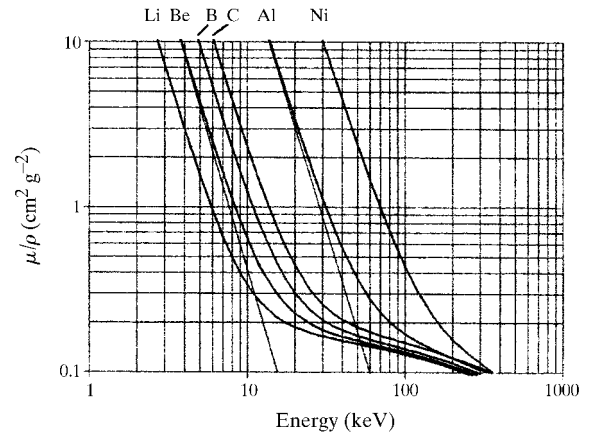

Figure 7
Mass attenuation coefficient μ/ρ for Li, Be, B, C, Al and Ni. For Be and Al the photoabsorption coefficent τ/ρ is also shown (thin lines) (Henke *et al.*, 1993).

lens aperture. With $2k_1^2R^2 = (4.58 \pm 0.23) \times 10^{14}$, $\sigma_v = 14.9\,\mu m$ and $\sigma_h = 297\,\mu m$ we calculate a spot size $B_v = 0.9 \pm 0.1\,\mu m$ in the vertical and $B_h = 14.2 \pm 1.4\,\mu m$ in the horizontal. The intensity was measured with a detector which had a point spread function of $1.2 \pm 0.1\,\mu m$ FWHM (Koch *et al.*, 1998). So, the expected overall spot size is $1.5 \pm 0.1\,\mu m$ in the vertical and $14.3 \pm 1.4\,\mu m$ in the horizontal. Fig. 8 shows the experimental result with a horizontal and a vertical scan. The measured spot size is $1.6 \pm 0.3\,\mu m \times 14.1 \pm 0.3\,\mu m$, in good agreement with the expected result. Note that the rugged structure in the horizontal line scan is not noise but reflects structure in the incoming intensity, which we believe is due to the effect of windows, absorbers and the monochromator crystals.

The transmission of the lens considered here ($d = 16 \pm 2\,\mu m$) is $T_p = 0.53 \pm 0.16\%$. The theoretical gain of the lens is 200 ± 40 compared with an experimental value of 177 ± 35. The great advantage of beryllium over aluminium becomes visible in the transmission, *e.g.* a beryllium lens with $N = 52$ has $f = 1.28\,m$ at 15 keV. When all geometrical parameters are kept the same, then $\mu = 0.52\,cm^{-1}$, $a = 0.64$ and $a_p = 1.60$. The effective aperture now becomes $633\,\mu m$ and the transmission is 30%, an increase by a factor of 60 compared with aluminium. The gain compared with a pinhole of equal size would be 11 800.

3.2.5. *Intensity on the optical axis G = 0.* On the optical axis the intensity is distributed over a much larger range in
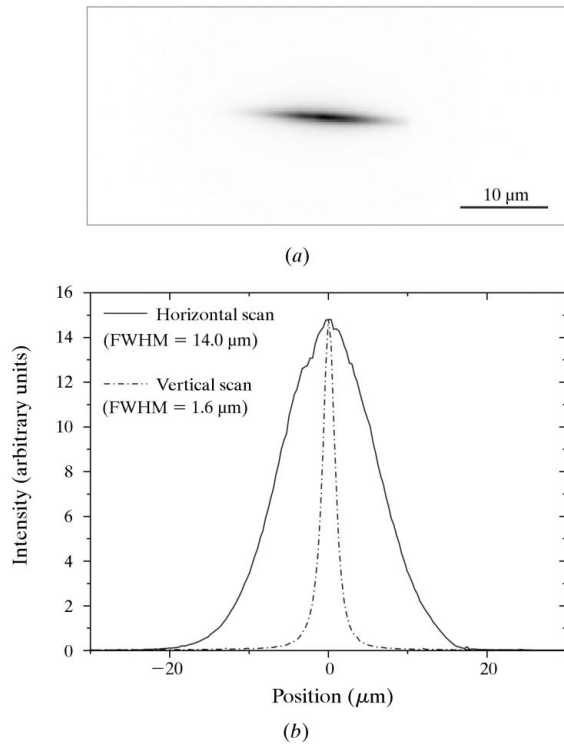

(a)

(b)

Figure 8
ID22 undulator source of the ESRF imaged by an aluminium CRL with 15 keV photon energy (*a*) and linear scans in the horizontal and vertical directions resulting in a $14.1 \times 1.6\,\mu m^2$ spot size (FWHM) (*b*).

space. The longitudinal distribution on the ray $G = 0$ has, according to equation (42), a FWHM B_l given by

$$B_l = [L_{20}^2(2a)^{1/2}/k_1R^2]$$
$$\times [(a_v^2 + a_h^2 + 14a_va_h)^{1/2} - (a_v + a_h)]^{1/2}, \quad (51)$$

with a_v and a_h given in equation (43).

In the case of the aluminium lens described in the previous section, $B_l = 44.8\,mm$. This is a very large depth of field, which is typical for refractive X-ray lenses and which is mainly due to the small effective aperture of the lens.

3.2.6. *Laterally coherent secondary source.* Coherent X-ray scattering is a new spectroscopy for studying dynamical processes, which extends speckle spectroscopy with laser light from the µm length scale to the nm range (Brauer *et al.*, 1995; Thurn-Albrecht *et al.*, 1996; Mochrie *et al.*, 1997). The spectroscopy needs a laterally coherent X-ray beam. The CRLs are excellently suited to generate a secondary source with this property if they are installed at an undulator at third-generation synchrotron radiation sources. According to Fig. 9 the CRL generates an image of the source which illuminates an area of dimension d_{ill} on the sample,

$$d_{ill} = D_{eff}\,L_3/L_2. \quad (52)$$

On the other hand, the lateral coherence length of the secondary source at the position of the sample is

$$l_{tr} = \lambda\,L_3/B_v^{dem}, \quad (53)$$

where $B_v^{dem} \equiv d_v\,L_2/L_1$ is the size of the secondary source given by the demagnification by the lens. The sample is coherently illuminated if $d_{ill} \leq l_{tr}$, *i.e.* if

$$B_v^{dem} \leq (\lambda/D_{eff})L_2 \equiv B_v^{diff}. \quad (54)$$

In other words, when diffraction limits the size of the secondary source, then this source can be considered as a point source which illuminates the sample coherently in the lateral direction. Equation (54) may also be written as

$$D_{eff} \leq \lambda L_1/d_v. \quad (55)$$

For $\lambda = 1$ Å, $L_1 = 63\,m$ and $d_v = 2.355\sigma_v = 35\,\mu m$, this gives $D_{eff} \leq 180\,\mu m$. In the vertical direction this condition is fulfilled for the aluminium CRL described in this paper. In the horizontal plane, however, the secondary source is not diffraction limited. Additional means have to be found to
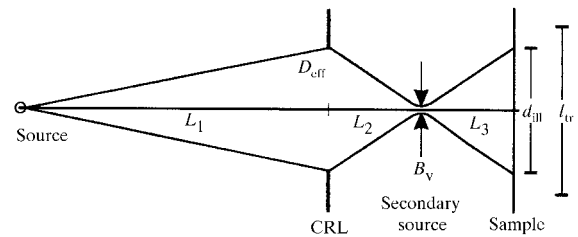

Figure 9
Set-up for generating a laterally coherent secondary X-ray source, which illuminates an object coherently.

reduce the effective source in the horizontal in order to illuminate the sample coherently in both directions.

3.2.7. *Highly parallel X-ray beam generated by CRL.* The beam emitted by an undulator has already a small divergence of typically 25 µrad and generates a spot size of ~1 mm at 40 m from the source. By means of a refractive lens the beam can be made even less divergent, when the source is in the focal spot of the lens. For a single aluminium lens ($N = 1$) at 15 keV with $\delta = 2.41 \times 10^{-6}$ the focal length is 41.43 m. This is a typical value for the distance between the undulator and the first experimental hutch at ESRF beamlines. For a single beryllium lens ($N = 1$) with $\delta = 2.37 \times 10^{-6}$ at 12 keV the focal length is 42.24 m. In both cases R was assumed to be 0.2 mm. When $N = 1$, the absorption parameter $a_p = aR_0^2/2R^2$ is small (*e.g.* it is 1.03 for aluminium at 15 keV), and it is no longer appropriate to replace the upper integration boundary in equation (26) by infinity. It is somewhat tedious to solve the integrals for calculating the intensity distribution. However, the main results on the beam divergence are evident in the light of the results from the previous sections. When the source is in the focal spot of a single lens, the beam divergence is

$$\Delta\theta_v = [(d_v/L_1)^2 + (1.029\lambda/D_{\text{eff}})^2]^{1/2}, \qquad (56)$$

and a corresponding expression exists for $\Delta\theta_h$. The first term is due to the finite source size and the second is due to diffraction at the effective aperture D_{eff} given by equation (46). A single aluminium lens at 15 keV with $a = 0.41$, $f = L_1 = 41.43$ m, $D_{\text{eff}} = 708$ µm, has a divergence $\Delta\theta_v = 0.85$ µrad which is at least a factor of 20 smaller than the divergence of the undulator without lens. In the horizontal the reduction in divergence is less dramatic with $\Delta\theta_h = 16.8$ µrad. In both cases it is the source size which determines the beam divergence behind the lens.

3.2.8. *Imaging of an X-ray free-electron laser source by a CRL.* There are plans to build an X-ray free-electron laser (XFEL) based on the self-amplified-spontaneous-emission (SASE) principle (Ingelman & Jonsson, 1997). It is hoped that the laser will emit a laterally coherent X-ray beam in the TEM$_{00}$ mode, which is a Gaussian delimited spherical wave. The divergence is expected to be 1 µrad. At a distance of 1000 m an object of 1 mm in diameter is laterally coherently illuminated. A typical wavelength of this source will be 1 Å (Schneider, 1997). Under these conditions the source can be considered as a point source ($\sigma_v = \sigma_h = 0$), although the geometrical source is 50 µm in diameter. According to equation (44) the image of the source will have a transverse FWHM B_{tr} of

$$B_{\text{tr}} = 0.75(\lambda L_{20}/2R)(a/2)^{1/2} = 0.75(\lambda L_{20}/D_{\text{eff}}), \qquad (57)$$

given by the diffraction at the effective aperture of the lens. For a beryllium CRL with $N = 45$ individual lenses at 12.4 keV ($\delta = 2.22 \times 10^{-6}$, $\mu = 0.70$ cm^{-1}, $\sigma = 0.2$ µm, $d = 20$ µm) we obtain a focal length of $f = 1$ m. The parameter a_p is 1.75. This results in a transmission of 26%, an effective aperture of $D_{\text{eff}} = 614$ µm, a focal spot size of $B_{\text{tr}} = 0.12$ µm and a gain of ~10^7.

4. Imaging of an object illuminated by an undulator beam by means of a CRL

4.1. *Theory of imaging*

In this section we consider the concept of a microscope working in the hard X-ray regime between ~5 and 60 keV. Fig. 10 shows a schematic set-up. The object, illuminated by the undulator, is characterized by a transmission function $T(x, y)$. For a thin slab of thickness D in the beam direction with index of refraction $n(x, y, z)$, $T(x, y)$ reads

$$T(x, y) = \exp\left[ik \int_0^D dz\, n(x, y, z) - 1 \right]. \qquad (58)$$

The object is located slightly outside of the focal length f of the CRL ($L_1 > f$). Then the lens images the object in the image plane at a distance $L_{20} = f L_1/(L_1 - f)$ on a high-resolution detector. The magnification of the image is

$$1/m = L_{20}/L_1. \qquad (59)$$

At the beamline ID22, L_{20} may be chosen as large as 25 m. For a focal length of 1 m this results in a magnification of at least 20. The main advantage of this magnification is in the relaxed requirements on the detector. We will see that the resolving power of the microscope may be as good as 0.1 µm. However, there is no detector available with this resolution. Our high-resolution detector (Koch *et al.*, 1998) has a point spread function of ~1 µm FWHM and is, owing to the magnification, able to resolve details in the object below 0.1 µm in size.

We now calculate the intensity distribution in the detector, in a similar way as performed in §3. The divergence of the X-ray beam emitted by the undulator is about 25 µrad. The distance L to the object is typically 42 m at the ESRF. As a consequence, every source point illuminates every object point when the object is below 1 mm in diameter. The field amplitude at the exit of the illuminated object in the point (x, y) is

$$\Phi(x, y) = \exp[-i(\omega t - k_1 L)]T(x, y)$$
$$\times \sum_{jk} \exp\Big\{ i[(X_j - x)^2/2L + i\Psi_v(X_j t)$$
$$+ i[(Y_k - y)^2/2L + i\Psi_h(Y_k t) \Big\}. \qquad (60)$$

This amplitude has to be transferred through the lens to the observation point P in the detector plane, in a similar way as performed in §3. The amplitude at the point P at time t is
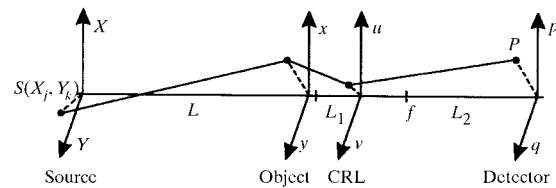

Figure 10
Set-up for a hard X-ray microscope with coordinate system used in the text.

$$\Phi(p, q, t) = (\pi\Delta/\alpha)\exp\{-i\omega t + ik_1[L + L_1 + L_2$$
$$+ (p^2 + q^2)/2L_2]\}\sum_{jk} N_{jk}, \tag{61}$$

$$N_{jk} = \int dx\, dy\, K_v(X_j, x, t)K_h(Y_k, y, t)T(x, y),$$

with

$$K_v = \exp\{i\Psi_v(X_j, t) + ik_1[(X_j - x)^2/2L + x^2/2L_1]$$
$$- (k_1^2\alpha^*/4|\alpha|^2)(x/L_1 + p/L_2)^2\}, \tag{62}$$

and similarly for K_h.

The intensity measured in the detector is proportional to $\langle|\Phi_p(pqt)|^2\rangle$ with the detector average given by equation (7). This expression contains the integral

$$(1/T)\int_{-T/2}^{T/2} dt\, \exp[-i\Psi_v(X_j t) - i\Psi_v(X_{j'} t)] = (2\pi/T)\delta_{jj'}. \tag{63}$$

As in §3, the Kronecker delta is a consequence of the long detection time $T \gg \tau_0$. A similar Kronecker delta is obtained for the summation over k and k'. The summation over the source points j (and k) is replaced by integration over a Gaussian distribution, giving

$$\sum_j \exp\{-ik_1[(x - x')/L]X_j\}$$
$$= (2\pi\sigma_v^2)^{-1/2}\int_{-\infty}^{\infty} dX\, \exp(-X^2/2\sigma_v^2)$$
$$\times \exp\{-ik_1[X(x - x')/L]\}$$
$$= \exp[-(x - x')^2/2l_v^2], \tag{64}$$

where

$$l_v = \lambda L/2\pi\sigma_v = \lambda L/\{\pi/[(2\ln 2)^{1/2}]d_v\} \tag{65}$$

is the transverse coherence length in the x-direction. A similar value is defined for the y-direction. Two points x and x' in the object are illuminated coherently by the source if $|x - x'| \ll l_v$. In that case the field amplitudes emitted by these two points have a fixed phase relation. We thus obtain for the intensity,

$$(|\alpha|^2/\pi^2\Delta^2)\langle|\Phi_P(p, q)|^2\rangle =$$
$$\int dx\, dx'\, dy\, dy'\hat{K}_v(x, x')\hat{K}_h(y, y')T(x, y)T^*(x', y'), \tag{66}$$

with

$$\hat{K}_v(x, x') = \exp[-(x - x')^2/2l_v^2]$$
$$\times \exp[i(k_1/2)(1/L + 1/L_1)(x^2 - x'^2)]$$
$$\times \exp\{(-k_1^2/4|\alpha|^2)[\alpha^*(x/L_1 + p/L_2)^2$$
$$+ \alpha(x'/L_1 + p/L_2)^2]\}, \tag{67}$$

and the corresponding expression for $\hat{K}_h$.

We now have to consider the object more in detail. If the object is of unknown structure, we may determine its structure by imaging it by means of our hard X-ray microscope and by reconstructing the three-dimensional distribution $n(x, y, z)$ in equation (58) *via* a tomographic approach. Techniques have been developed for how this may be performed (Gilboy, 1995; Grodzins, 1983; Snigirev *et al.*, 1995; Raven *et al.*, 1996, 1997; Spanne *et al.*, 1999; Momose, 1995; Beckmann *et al.*, 1997). Here, we would like to consider the transversal and longitudinal resolving power of our microscope. For that purpose we assume that the object is a non-transparent screen with two pinholes at the positions $(x_0, 0)$ and $(-x_0, 0)$ along the x-axis,

$$T(x, y) = [\delta(x - x_0) + \delta(x + x_0)]\delta(y). \tag{68}$$

The integrals in equation (66) can now be solved analytically, giving

$$\langle|\Phi_P(p, q)|^2\rangle = \frac{(2\pi R^2)^2\Delta^2}{a^2 + b^2F^2}\exp\left\{-k_1^2R^2/a^2 + b^2F^2 a\frac{q^2}{L_2^2}\right\}$$
$$\times 2\exp\left\{-\frac{k_1^2R^2}{a^2 + b^2F^2}a\left(\frac{x_0^2}{L_1^2} + \frac{p^2}{L_2^2}\right)\right\}$$
$$\times \left\{\cosh\left(\frac{k_1^2R^2}{a^2 + b^2F^2}\cdot\frac{2x_0 a}{L_1 L_2}p\right)\right.$$
$$+ \exp\left[-\frac{(2x_0)^2}{2l_v^2}\right]$$
$$\times \left.\cos\left(\frac{k_1^2R^2}{a^2 + b^2F^2}\frac{2x_0 bF}{L_1 L_2}p\right)\right\}. \tag{69}$$

We will first consider two extreme regimes, that of incoherent and that of coherent illumination of the object.

4.1.1. *Incoherent illumination:* $2x_0 \gg l_v$. If the lateral coherence length is very small ($2x_0 \gg l_v$), then the second term in the wavy brackets [equation (69)] is negligible and the intensity in the focal plane $F = 0$ is proportional to

$$\langle|\Phi_P(p)|^2\rangle \simeq \exp[(-k_1^2R^2/a)(p/L_2 0 + x_0/L_1)^2]$$
$$+ \exp[(-k_1^2R^2/a)(p/L_{20} - x_0/L_1)^2]. \tag{70}$$

The intensity is given by two Gaussians (Fig. 11) at a distance $2x_0 L_{20}/L_1$. We define as transverse resolving
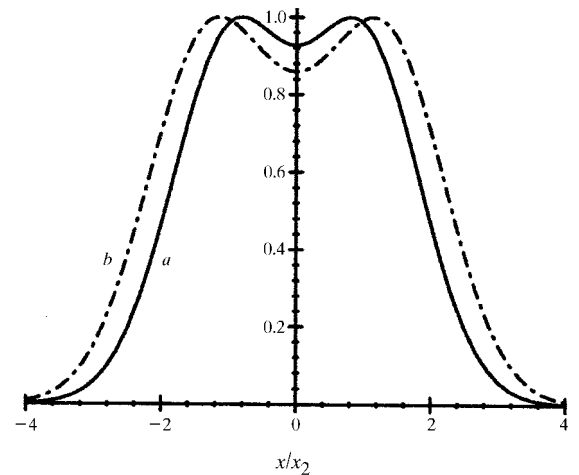

Figure 11
Intensity distribution for two object points at distance $2x_0$ illuminated incoherently (*a*) and coherently (*b*).

power d_t that distance $2x_0$ in the object for which the image points are separated by the FWHM of each image. This gives

$$d_t^{\text{inc}} = [2(2\ln 2)^{1/2}/\pi](\lambda L_1/D_{\text{eff}})$$
$$\cong 0.75(\lambda L_1/D_{\text{eff}}) = 0.75(\lambda/2\text{NA}), \qquad (71)$$

where NA is the numerical aperture,

$$\text{NA} = D_{\text{eff}}/2L_1. \qquad (72)$$

In the present calculation we have assumed R_0 to be very large, then $D_{\text{eff}} = 2R(2/a)^{1/2}$. When a_p is not large, then D_{eff} is given by equation (46). The intensity at $p = 0$ is 93.7% of the value at the maxima (Fig. 11). For the case of the aluminium CRL at 15 keV mentioned in §3.2.4 ($N = 33$, $f = 1.26$ m, $a_p = 32.12$ and $D_{\text{eff}} = 154$ μm) and an object-to-lens distance of $L_1 = 1.36$ m, the resolving power is 0.55 ± 0.01 μm and the numerical aperture is NA $= 95.66 \pm 0.08 \times 10^{-5}$. It is the low NA ('slender' X-ray optics) which is responsible for the resolution being much larger than the photon wavelength. Nevertheless, a value of $d_t = 0.14$ μm can be achieved with an aluminium CRL at 40 keV when the transmission in aluminium is improved compared with the value at 15 keV.

The low value of the NA results in a very poor longitudinal resolving power d_l of the hard X-ray microscope. Indeed, for $p = q = 0$ and $x_0 = 0$,

$$\langle|\Phi_P(L_2)|^2\rangle = (2\pi R^2)^2 \Delta^2/(a^2 + b^2 F^2). \qquad (73)$$

The longitudinal resolving power d_l is defined as the distance of two object points along the optical axis whose image distance is as large as the spread of one image point along the optical axis.

$$d_l = 2(a/b)L_1^2 = (8/\pi)\lambda(L_1^2/D_{\text{eff}}^2) = (2/\pi)\lambda(1/(\text{NA})^2). \qquad (74)$$

In the case of the aluminium CRL with $N = 33$ at 15 keV, $d_l = 16.5 \pm 0.1$ mm. Note that d_t is proportional to the inverse NA whereas d_l is proportional to the square of the inverse NA as is well known in optics (Lipson *et al.*, 1998).

4.1.2. *Coherent illumination:* $2x_0 \ll l_\nu$. If the lateral coherence length is large ($2x_0 \ll l_\nu$), then the second term in the wavy brackets [equation (69)] is 1 for $F = 0$ and the intensity in the focal plane is proportional to

$$\langle|\Phi_P(p)|^2\rangle = \left\{\exp\left[-\frac{k_1^2 R^2}{2a}\left(\frac{p}{L_{20}} - \frac{x_0}{L_1}\right)^2\right]\right.$$
$$\left. + \exp\left[-\frac{k_1^2 R^2}{2a}\left(\frac{p}{L_{20}} + \frac{x_0}{L_1}\right)^2\right]\right\}^2. \qquad (75)$$

Fig. 11 shows the intensity distribution for coherent and incoherent illumination. If the resolving power is defined again by the separation of the amplitude peaks being equal to the FWHM of an amplitude peak we find

$$d_t^{\text{coh}} = 2^{1/2} d_t^{\text{inc}} = 1.06 \lambda L_1/D_{\text{eff}} = 1.06(\lambda/2\text{NA}). \qquad (76)$$

In that case the indentation at $p = 0$ is 14.0%. It is well known from optics that incoherent illumination improves the lateral resolution (Lipson *et al.*, 1998).

4.2. *Comparison with the experiment*

We have imaged a few objects with the new CRL. The object is illuminated from behind by the X-ray source and imaged through the lens onto a position-sensitive detector. Due to the low absorption of hard X-rays in air there is no need for a sample chamber nor for evacuated beam pipes. However, the latter might be useful in order to reduce the background due to Compton scattering in air. In Fig. 12(a) is shown the X-ray microscopical image of a double gold mesh. It consists of a square mesh with a period of 15 μm, a bar width of 3 μm and a thickness of 2 μm. Attached from behind in one part of this mesh is a second linear mesh with a period of 1 μm, a width of 0.5 μm and a thickness of 0.5 μm.

The mesh was imaged with 23.5 keV (0.53 Å) photons from ID22. The aluminium lens and imaging parameters were $N = 62$, $f = 1.65 \pm 0.04$ m, $L_1 = 1.79 \pm 0.01$ m, $L_{20} = 21.40 \pm 0.04$ m, $\mu = 5.81$ cm^{-1}, $D_{\text{eff}} = 211 \pm 9$ μm. An area of 300 μm in diameter was imaged with a magnification of 12 ± 0.1 and a theoretical lateral resolving power of $d_t = 0.34 \pm 0.02$ μm. Note that the image shows almost no distortion over the field of view. Fig. 12(b) shows an enlargement of the region inside the rectangle of Fig. 12(a). For comparison, part of the mesh has been imaged with a scanning electron microscope. Note that the wires behind the bars of the coarse grid are visible in the X-ray microscope but not in the electron microscope. This illustrates the imaging possibilities of opaque objects by the new hard X-ray microscope.

For testing the resolution of the new microscope we have imaged a Fresnel zone plate (Lai *et al.*, 1992) with 169 zones made of gold (1.15 μm thick on a Si$_3$N$_4$ substrate of 0.1 μm thickness). The outermost zones had a width of 0.3 μm. Fig. 13 shows an enlarged region which includes the border of the Fresnel lens. The parameters of the lens and the photon energy were the same as those from Fig. 12. The outermost zones of the Fresnel lens are clearly resolved and the experimentally achieved resolution is in good agreement with the expected resolution of 0.34 μm resulting from diffraction at the finite aperture of the lens. Figs. 12 and 13 were recorded on Kodak high-resolution X-ray film which had a resolution of 1 μm. The smallest image structures were about 3 μm (which correspond to object structures of 0.25 μm at a magnification of 12). Thus the resolution of the whole set-up was not limited by that of the film.
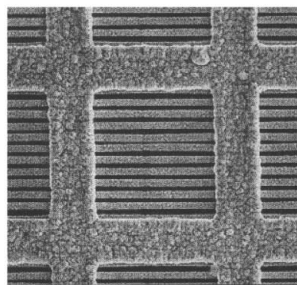
4.3. *Limits of the lateral resolving power*

As outlined in equations (71) and (72) the lateral resolution d_t is limited by the small value of the numerical aperture NA, which is ultimately limited by the attenuation of the X-rays in the lens material. Fig. 14 shows the variation of d_t with photon energy E for aluminium and beryl-
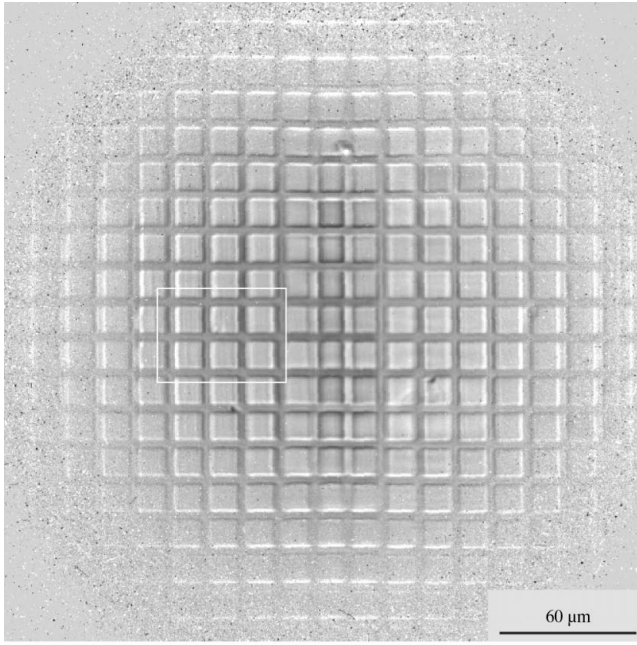
(a)
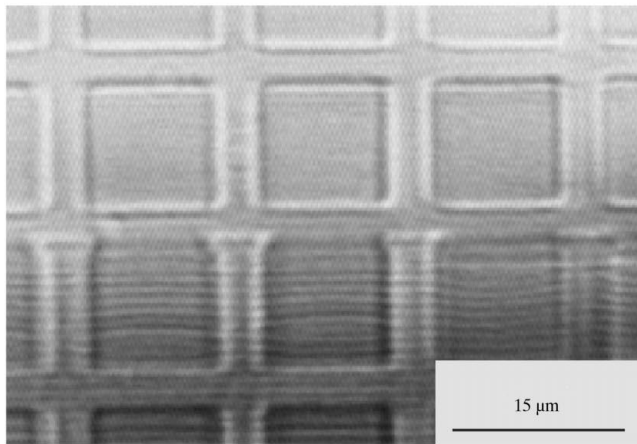
(b)

(c)

Figure 12
X-ray image of a square gold mesh with a period of 15 μm in both directions. The photon energy was 23.5 keV. (a) Full field of view; (b) enlargement of (a) with the lower squares having attached to them a second linear gold mesh with period 1 μm; (c) scanning electron micrograph of one square from (a) and (b). Note that the electron micrograph in contrast to the X-ray micrograph is not able to show the linear gold grid behind the bars of the coarse gold lattice.

lium CRL under the following assumptions: $f = 1$ m, $R = 0.2$ mm, $2R_0 = 0.87$ mm. Also shown are the number N of individual lenses in the stack and the transmission of the lens (with $d = 10$ μm for aluminium and $d = 20$ μm for beryllium).

We expect a resolution better than 0.1 μm in the case of beryllium above 15 keV. As shown in Fig. 7 it is Compton scattering which ultimately limits the resolution and the transmission in beryllium. Without Compton scattering we would expect a lateral resolution of 0.05 μm for a beryllium CRL with $f = 1$ m at 20 keV and a transmission above 50%. Since Compton scattering cannot be avoided, the question arises if there are other ways to increase the effective
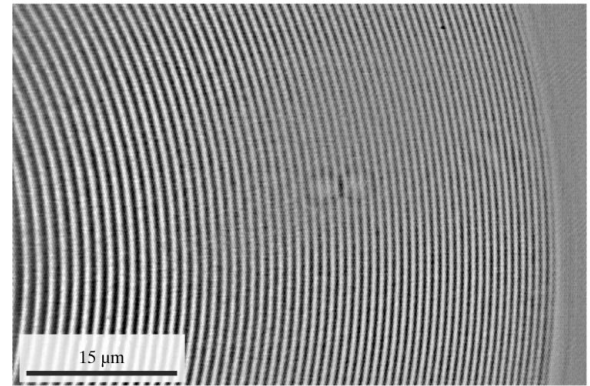

Figure 13
X-ray micrograph (23.5 keV) of a Fresnel zone plate with 169 gold zones on a Si_3N_4 substrate. The outermost zone of width 0.3 μm is clearly resolved.
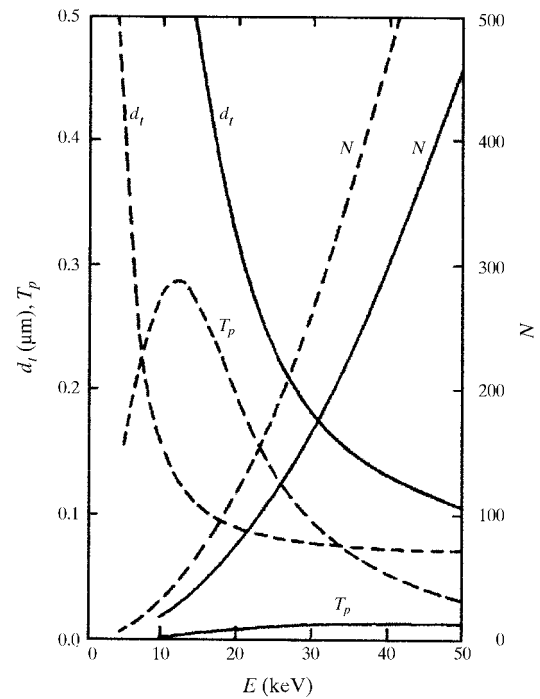

Figure 14
Lateral resolution d_t, number N of individual lenses and transmission T_p of aluminium (full line) and beryllium (dashed line) CRL with 1 m focal length *versus* photon energy E.

aperture and thus the resolution. A possibility is shown in Fig. 15. It is a parabolic refractive lens with kinoform profile,

$$w = (s^2/2R) - MW, \tag{77}$$

where M is an integer. For $W = 0$, equation (77) is just the parabolic profile discussed up to now. The discontinuity W in the profile reduces the geometrical path in the lens material. Hence, it also reduces attenuation. There is no necessity, as in a usual Fresnel construction, to choose W in such a way that the path difference between neighbouring sections is λ. It can just as well be $m\lambda$ where m is a large integer, so that $2s_1 \simeq D_{\mathrm{eff}}$. A typical value for m is 100. The profit from this choice is a low number of steps M, combined with an increase in the effective aperture by $(M + 1)^{1/2}$. However, there is a price to be paid. First, once W is fixed, the photon wavelength is fixed, which is a very serious handicap. Secondly, the requirements on the precision in the shape of the lens increase with m. At the present time it is not yet clear if this approach for increasing the effective apperture is technically feasible.

5. Conclusions

The results of this paper may be summarized as follows.

(i) Compound refractive X-ray lenses (CRLs) with parabolic profile have been constructed and successfully tested.

(ii) They can be used for hard X-rays up to ∼60 keV.

(iii) They have a geometric aperture of 1 mm and are best suited for undulator beams at synchrotron radiation storage rings.

(iv) They are stable in the white beam of an undulator.

(v) Due to their parabolic profile, CRLs are genuine imaging devices, similar to glass lenses for visible light.

(vi) We have developed the theory for imaging a source and an object illuminated by an X-ray source, including the effects of attenuation (photoabsorption and Compton scattering) and of surface roughness. The central expressions are equations (42) and (66).

(vii) The parabolic CRLs have been tested for imaging up to 41 keV. There is excellent agreement between theory and experiment. The surface finish of the lenses is good enough, so that surface roughness can be neglected.

(viii) A characteristic feature of CRLs for X-rays is their small aperture (below ∼500 μm) and their small numerical aperture (NA). Nevertheless a lateral resolution of 0.3 μm

has been achieved and a resolution below 0.1 μm can be expected. Compton scattering in the lens material limits the resolution.

(ix) The transmission ranges from a few % in aluminium CRLs up to ∼30% in beryllium CRLs.

(x) The main fields of application of refractive X-ray lenses with parabolic profile are as follows.

(*a*) Microanalysis with a beam in the μm range for diffraction, fluorescence, absorption, reflectometry. The small NA of the lens guarantees a good beam collimation of 0.3 mrad. Nevertheless, the gain of the lens is at least 100 for an aluminium CRL and is expected to be a few 1000 for a beryllium CRL. The 'pink' beam of an undulator harmonic ($\Delta E/E \simeq 1\%$) is transmitted through a CRL without loss of focusing.

(*b*) Imaging in absorption and phase contrast. Refractive X-ray lenses are complementary to other microscopical techniques. It is possible to image opaque objects which cannot tolerate sample preparation without changing the state of the sample. Examples are biological cells or soil samples which change structure and functionality when the water is removed. A hard X-ray microscope, on the other hand, allows for *in situ* investigation in the natural environment.

(*c*) Coherent X-ray scattering. In connection with a high-brilliance X-ray source a CRL can generate a secondary X-ray source which is diffraction limited (at least in the vertical direction at ESRF undulators). The sample area illuminated by the secondary source is then smaller than the coherence area (Fig. 9). In other words, the lens works like an aperture, without, however, reducing the intensity as does a pinhole. We expect CRLs to be helpful optical devices for speckle spectroscopy with hard X-rays.

APPENDIX *A*
Focal length of a CRL

The focal length of a CRL is calculated by means of Snell's law, as usual for refractive lenses. The curvature of the beam in the stack can be taken into account. However, it turns out that this effect is small as long as the length of the lens is short compared with the focal length. Within corrections of order δ, the focal length of a parabolic CRL with N individual lenses in the stack is found to be (Fig. 16)

$$f = (R/2N\delta)\big[1 - N\delta\big(1 - u_1^2/2R^2\big)\big], \tag{78}$$

as measured from the middle of the CRL. u_1 is the height where the incoming beam hits the first lens. The correction term (spherical aberration) is typically below 10^{-4} or 0.1 mm for a CRL with 1 m focal length. Due to the large depth of field of refractive X-ray lenses and due to the large distances L_1, L_2 and f, the correction can be neglected for all practical purposes and a parabolic CRL can be considered as free of spherical aberration.
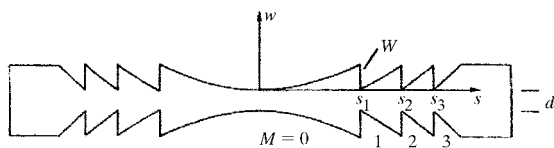
Figure 15
Parabolic refractive X-ray lens with kinoform profile as a possibility to increase the effective aperture of a CRL.

APPENDIX *B*
Transmission amplitude t_{12} for a vacuum–lens interface

We consider the transmission of an X-ray through a vacuum–lens interface, as illustrated in Fig. 16. In the right-handed coordinate system (u', v', w') the incoming and transmitted wave vectors $\mathbf{k}_1$ and $\mathbf{k}_2$ have the components

$$\mathbf{k}_1 = k_1(-\cos\theta_1, 0, \sin\theta_1) \tag{79}$$

and

$$\mathbf{k}_2 = n_2 k_1(-\cos\theta_2, 0, \sin\theta_2). \tag{80}$$

Due to Snell's law,

$$\cos\theta_1 = n_2\cos\theta_2, \tag{81}$$

the momentum transfer Q for transmission has only a w' component,

$$Q = k_1(n_2\sin\theta_2 - \sin\theta_1). \tag{82}$$

For the low-Z materials of interest in X-ray lenses and for hard X-rays, the absorptive correction β of the index of refraction is about three orders of magnitude smaller than the dispersive correction δ (see Table 1). Hence, we neglect the absorption in the transmission amplitude t_{12} and obtain

$$n_2\sin\theta_2 = \sin\theta_1 - \delta/\sin\theta_1, \tag{83}$$

$$Q = -k_1\delta/\sin\theta_1, \tag{84}$$

with δ typically 10^{-6}. Note the very low value of the momentum transfer. We saw in the main body of this paper that this low value is at the origin of the insensitivity of refractive X-ray lenses to surface roughness, a feature in which X-ray lenses and mirrors differ drastically. The angle
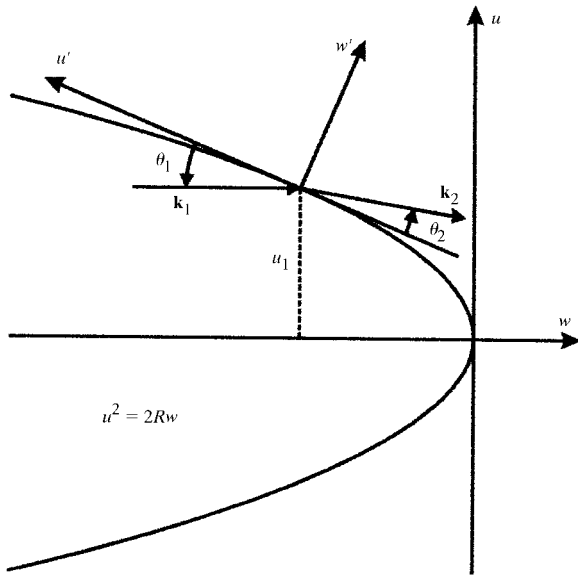

Figure 16
Notations for calculating the focal length and the transmission of a CRL.

θ_1 varies with the height u from the optical axis in the parabolic lens $u^2 = 2Rw$ according to

$$1/\sin^2\theta_1 = 1 + u^2/R^2, \tag{85}$$

so that

$$Q = -k_1\delta(1 + u^2/R^2)^{1/2} = -Q_0(1 + u^2/R^2)^{1/2}, \tag{86}$$

$$Q_0 = k_1\delta.$$

Let us consider the transmission of s-polarized X-rays through the interface. The tangential components of the $\mathbf{E}$ and $\mathbf{H}$ fields have to be continuous. This results in the following condition for the amplitudes A_2 and A_1 of the transmitted and incoming waves,

$$A_2/A_1 = t_{12} = [2\sin\theta_1/(\sin\theta_1 + n_2\sin\theta_2)]\langle\exp(iQ\eta)\rangle. \tag{87}$$

The first factor is the usual Fresnel transmission amplitude, as explained in optics books (Lipson *et al.*, 1998). In the present case it is 1 with an accuracy of $\delta/2\sin^2\theta_1$, which is $\sim 10^{-6}$, as can be seen from equation (83). The second factor is due to interface roughness. In the Rayleigh model of roughness (Stanglmeier *et al.*, 1992) the interface is described by a set of parallel surfaces displaced by η from the average surface and distributed around the average surface according to a Gaussian distribution

$$w(\eta) = (2\pi\sigma^2)^{-1/2}\exp(-\eta^2/2\sigma^2). \tag{88}$$

$Q\eta$ is the phase shift of the wave transmitted through the surface at η compared with a wave transmitted at $\eta = 0$. Averaging over the distribution gives

$$\langle\exp(iQ\eta)\rangle = \exp(-Q^2\sigma^2/2)$$
$$= \exp[-Q_0^2\sigma^2(1 + u^2/R^2)/2]. \tag{89}$$

Hence,

$$t_{12} = \exp(-Q_0^2\sigma^2/2)\exp(-Q_0^2\sigma^2 u^2/2R^2). \tag{90}$$

The transmission amplitude t_{21} for the beam leaving the lens has the same value. Since the roughnesses on both sides of a lens are uncorrelated, as are the roughnesses for different lenses, the amplitude for the transmission through $2N$ interfaces of N lenses in a stack is

$$(t_{12}t_{21})^N = \exp(-NQ_0^2\sigma^2)\exp(-NQ_0^2\sigma^2 u^2/R^2). \tag{91}$$

Within the accuracy $O(\delta) \simeq 10^{-6}$ the same result is obtained for p-polarized X-rays.

References

Abramowitz, M. & Stegun, I. (1972). *Handbook of Mathematical Functions*. New York: Dover.

Aristov, V., Snigirev, A., Basov, Y. & Nikulin, A. (1986). *AIP Conf. Proc.* **147**, 253.

Beckmann, F., Bonse, U., Busch, F. & Gunnewig, O. (1997). *J. Comput. Assisted Tomogr.* **21**, 539–553.

Bilderback, D., Hoffman, S. & Thiel, D. (1994). *Science*, **263**, 201–203.

Brauer, S., Stephenson, G., Sutton, M., Brüning, R., Dufresne, E., Mochrie, S.-J., Grübel, G., Als-Nielsen, J. & Abernathy, D. (1995). *Phys. Rev. Lett.* **74**, 2010.

Elleaume, P. (1998). *J. Synchrotron Rad.* **5**, 1–5.

Eskildsen, M., Gammel, P., Isaacs, E., Detlefs, C., Mortensen, K. & Bishop, D. (1998). *Nature (London)*, **391**, 563.

Gilboy, W. (1995). *Appl. Radiat. Isot.* **46**, 689.

Grodzins, L. (1983). *Nucl. Instrum. Methods Phys. Res.* **206**, 547–552.

Hartman, Y., Tarazona, E., Elleaume, P., Snigireva, I. & Snigirev, A. (1995). *Rev. Sci. Instrum.* **66**(2), 1978–1980.

Henke, B., Gullikson, E. & Davis, J. (1993). *Atom. Data Nucl. Data Tables*, **54**, 181–342.

Hoffman, S., Thiel, D. & Bilderback, D. (1994). *Nucl. Instrum. Methods*, A**347**, 384.

Ingelman, G. & Jonsson, L. (1997). *Nucl. Instrum. Methods Phys. Res. A*, **398**, 1–107.

Jackson, J. (1975). *Classical Electrodynamics*. New York/London: Wiley.

James, R. W. (1967). *The Optical Principles of the Diffraction of X-rays.* Cornell University Press.

Kirkpatrick, P. & Baez, A. (1948). *J. Opt. Soc. Am.* **38**(9), 766–774.

Koch, A., Raven, C., Spanne, P. & Snigirev, A. (1998). *J. Opt. Soc. Am.* A**15**(7), 1940–1951.

Lai, B., Yun, W., Legnini, D., Xiao, Y., Chrzas, J., Viccaro, P. J., White, V., Bajikar, S., Denton, D. & Cerrina, F. (1992). *Appl. Phys. Lett.* **61**(16), 1877–1879.

Lengeler, B., Schroer, C., Richwin, M., Tümmler, J., Drakopoulos, M., Snigirev, A. & Snigireva, I. (1999). *Appl. Phys. Lett.* **74**, 3924–3926.

Lengeler, B., Tümmler, J., Snigirev, A., Snigireva, I. & Raven, C. (1998). *J. Appl. Phys.* **84**, 5855–5861.

Lipson, S., Lipson, H. & Tannhauser, D. (1998). *Optical Physics*, 3rd ed. Cambridge University Press.

Loudon, R. (1983). *The Quantum Theory of Light.* Oxford: Clarendon Press.

Mochrie, S.-J., Mayes, A., Sandy, A., Sutton, M., Brauer, S., Stephenson, G., Abernathy, D. & Grübel, G. (1997). *Phys. Rev. Lett.* **78**, 1275.

Momose, A. (1995). *Nucl. Instrum. Methods*, A**352**, 622–628.

Raven, C., Snigirev, A., Koch, A., Snigireva, I. & Kohn, V. (1997). *Proc. SPIE*, **3149**, 140–148.

Raven, C., Snigirev, A., Snigireva, I., Spanne, P., Souvorov, S. & Kohn, V. (1996). *Appl. Phys. Lett.* **69**(13), 1826–1828.

Schneider, J. (1997). *Nucl. Instrum. Methods Phys. Res. A*, **398**, 41–53.

Snigirev, A. (1995). *Rev. Sci. Instrum.* **66**(2), 2053–2058.

Snigirev, A., Filseth, B., Elleaume, P., Klocke, T., Kohn, V., Lengeler, B., Snigireva, I., Souvorov, A. & Tümmler, J. (1998). *Proc. SPIE*, **3151**, 164–170.

Snigirev, A., Kohn, V., Snigireva, I. & Lengeler, B. (1996). *Nature (London)*, **384**, 49–51.

Snigirev, A., Kohn, V., Snigireva, I., Souvorov, A. & Lengeler, B. (1998). *Appl. Opt.* **37**(4), 653–662.

Snigirev, A., Snigireva, I., Bösecke, P., Lequien, S. & Schelokov, I. (1997). *Opt. Commun.* **135**, 378–384.

Snigirev, A., Snigireva, I., Kohn, V., Kuznetsov, S. & Schelokov, I. (1995). *Rev. Sci. Instrum.* **66**(12), 5486–5492.

Snigireva, I., Souvorov, A. & Snigirev, A. (1998). *X-ray Microscopy and Spectroscopy.* Berlin, Heidelberg: Springer-Verlag.

Spanne, P., Raven, C., Snigireva, I. & Snigirev, A. (1999). *Phys. Med. Biol.* **44**(3), 741–749.

Stanglmeier, F., Lengeler, B., Weber, W., Göbel, H. & Schuster, M. (1992). *Acta Cryst.* A**48**, 626–639.

Suzuki, Y. & Uchida, F. (1992). *Rev. Sci. Instrum.* **63**(1), 578–581.

Tarazona, E., Elleaume, P., Hartman, Y., Snigirev, A. & Snigireva, I. (1994). *Rev. Sci. Instrum.* **65**(6), 1959–1963.

Thurn-Albrecht, J., Steffen, W., Patkowski, A., Meier, G., Fischer, E., Grübel, G. & Abernathy, D. (1996). *Phys. Rev. Lett.* **77**, 5437.

Underwood, J. (1986). *Rev. Sci. Instrum.* **57**(8), 2119–2123.

Underwood, J., Barbee, T. Jr & Frieber, C. (1986). *Appl. Opt.* **25**(11), 1730–1732.

Underwood, J., Thompson, A., Wu, Y. & Giauque, R. (1988). *Nucl. Instrum. Methods Phys. Res. A*, **266**, 296–302.

Yang, B. (1993). *Nucl. Instrum. Methods Phys. Res. A*, **328**, 578–587.

Yun, W., Lai, B., Lee, H.-R., Legnini, D., Rodrigues, W. & Smith, C. (1998). *J. Synchrotron Rad.* **5**, 1390–1395.